



AIAA-93-3411

**Application of the Shadowgraph Flow Visualization
Technique to a Full-Scale Helicopter Rotor in
Hover and Forward Flight**

Alexandra A. Swanson
Sterling Software
NASA Ames Research Center
Moffett Field, CA

**AIAA 11th
Applied Aerodynamics Conference
August 9-11, 1993 / Monterey, CA**

Application of the Shadowgraph Flow Visualization Technique to a Full-Scale Helicopter Rotor in Hover and Forward Flight

Alexandra A. Swanson*

Sterling Software

NASA Ames Research Center, Moffett Field, CA

Abstract*

The wide-field shadowgraph flow visualization technique was used for the first time with a full-scale helicopter rotor. This was accomplished during testing of a Sikorsky S-76 main rotor in the NASA Ames National Full-Scale Aerodynamics Complex (NFAC) 80- by 120-Foot Wind Tunnel. Hover, low-speed forward flight, and descent operating conditions were studied. Preliminary results are very promising with rotor wake tip vortices visible up to an advance ratio of 0.25. In addition, many details of the rotor wake were visible, including tip vortex roll-up, inboard wake vorticity, and flow unsteadiness due to test section recirculation effects in hover. Shadowgraphs of blade/vortex interactions were also acquired. Simultaneous top and side view shadowgraphs of the rotor wake were acquired by a newly developed synchronized digital imaging system. The imaging system proved to be a highly successful tool which made real-time examination of selected regions of the rotor wake possible.

Nomenclature

A_b rotor blade area, $NcR = \sigma A$, m^2

c blade chord, m

c_s speed of sound, m/sec

CT/σ rotor thrust coefficient normalized by solidity,
 $T/\rho A_b (\Omega R)^2$

M_{tip} rotor tip Mach number, $\Omega R/c_s$

N number of blades

r/R normalized radial distance from rotor center line

R rotor radius, m

T thrust, N

V_d rate of vertical descent, m/sec

V_∞ free stream wind speed, m/sec

z/R normalized axial distance from rotor tip path plane

α_s shaft angle of attack, deg

γ glide path angle, deg

μ rotor advance ratio, $V_\infty/\Omega R$

ρ density, kg/m^3

σ solidity, $Nc/\pi R$

Ψ_b blade azimuth location, deg

Ψ_w wake age, Ωt , deg

Ω rotor rotational speed, rad/sec

Introduction

Recent advances in the field of imaging technology now enable researchers to facilitate and conduct flow visualization work that previously was considered impossible. An innovative method for studying the time-dependent wake geometry of rotorcraft has been developed. The key to this new research capability is a high resolution imaging system with the ability to operate at various externally triggered frequencies and the capability of acquiring two simultaneous digital images in

* Aerospace Engineer. Member AIAA.

Copyright © 1993 by the American Institute of Aeronautics and Astronautics, Inc. No copyright is asserted in the United States under Title 17, U.S. Code. The U.S. Government has a royalty-free license to exercise all rights under the copyright claimed herein for Governmental purposes. All other rights are reserved by the copyright owner.

real time. This is important for acquiring quantitative wake geometry measurements and providing details on tip vortex roll-up and wake structure. Such information is crucial for the development and validation of accurate mathematical wake models for rotor aerodynamics and acoustic predictions.

Other flow visualization measurement techniques have major limitations when applied to large-scale rotor testing. Existing techniques such as laser Doppler velocimetry and particle tracking require seeding of the flow, which would be a very difficult and time-consuming undertaking in a large wind tunnel. Alternatively, Schlieren is not suited to large-scale flow visualization due to the size of mirrors required for large-scale testing. A final drawback of most previously studied rotor flow visualization techniques is the lack of real-time feedback. Image quality problems with still cameras are not known until the film is developed. This can cause significant delays in the test schedule. Also, with still cameras, the researcher is unable to survey the rotor wake for unexpected flow phenomena that may occur during a particular operating condition (e.g. blade/vortex interactions). Some rotor wake flow visualization studies have attempted the use of video equipment in order to acquire and review data in real time.^{1,2} However, standard video does not provide the high resolution image quality for rotor tests which require camera synchronization to a variable strobe frequency in low ambient light conditions.

Previous studies of the wide-field shadowgraph technique have yielded quantitative measurements of the wake geometry of small-scale rotors.¹⁻⁶ The shadowgraph technique has also demonstrated the potential for non-intrusive measurements of tip vortex core size.³ However, to date, the technique has not been applied to large- or full-scale rotors. A test was recently conducted to demonstrate the shadowgraph technique for a full-scale helicopter rotor system in the NASA Ames NFAC 80- by 120-Foot Wind Tunnel. No attempt was made to conduct a comprehensive survey of the rotor wake flow field. When preliminary tests showed promising results, available shadowgraph screens were positioned in order to acquire rotor wake geometry for the outer 25% of the rotor in the first quadrant of the rotor disk. Sample wake geometry results are presented for hover and forward flight (descent operating conditions) with empirical and analytical correlations. Shadowgraphs of repeatable blade/vortex interactions are also discussed and compared with acoustic noise measurements and wake geometry predictions. Additionally, details of the tip vortex roll-up and other tip vortex features are

presented. Finally, an example of simultaneous image capture is included.

Experimental Set-Up

A full-scale Sikorsky S-76 rotor was mounted on the Rotor Test Apparatus (RTA) in the NASA Ames NFAC 80- by 120-Foot Wind Tunnel as shown in Fig. 1. The four-bladed S-76 rotor has a 6.71 m (22 ft) radius, rotor solidity of 0.0747, and operates at a nominal tip speed of 206 m/s (675 ft/s) or $M_{tip}=0.605$. Complete S-76 rotor characteristics and further details on the full-scale test program are referenced.⁷

Figure 2 shows the experimental set-up for shadowgraph flow visualization and data acquisition. Further details on the wide-field shadowgraph technique are found in the literature.¹⁻⁶ One camera and strobe were positioned in a cavity of the wind tunnel ceiling for a top view of the S-76 rotor and a second camera and strobe were positioned in a cavity of the wind tunnel wall for a side view. Orthogonal positioning of cameras and strobes with respect to the rotor was not possible for all viewing positions in this test entry. Retroreflective screens were placed onto the wind tunnel wall and floor opposite the camera and strobe locations. Because this was the first attempt to conduct flow visualization on a full-scale rotor in a large wind tunnel test facility, a limited number of retroreflective screens were used. Minimizing the expense associated with purchasing large quantities of retroreflective sheeting and the time associated with installing numerous screens to the inside of the test section were the primary reasons for limiting the number of screens.

The components of a specially developed synchronized imaging system, as illustrated in Fig. 2, included: an azimuth synchronization box designed to deliver the desired shifted azimuth trigger pulse to a computer control unit; a computer control unit designed to send an external trigger to the strobes and cameras; two high resolution charge injection device (CID) cameras capable of synchronized operation from an external trigger; two monitors for real-time viewing of shadowgraph images; and two frame grabber boards and software written to drive the boards for data acquisition and storage of shadowgraph images at synchronized operating rates.

A comprehensive analytical code for rotorcraft, CAMRAD/JA⁸, was used to calculate nonuniform inflow free wake geometry for each test condition. A second program⁹ was then used to sort through and extract the

conditions for which a close blade/vortex interaction (BVI) occurred from the CAMRAD/JA free wake output. A close interaction was defined as a $0.10R$ vertical distance spacing between the vortex filament and the blade element. These wake geometry predictions were used to facilitate the placement of available shadowgraph screens for optimum viewing of blade/vortex interactions. In some limited instances, the screens were moved around in order to examine different regions of the rotor wake.

Shadowgraphs were acquired for various combinations of advance ratios ($0 < \mu < 0.25$), tip Mach numbers ($0.10 < M_{tip} < 0.61$), shaft angles ($-15 \text{ deg} < \alpha_s < 10 \text{ deg}$), and thrust conditions ($0.03 < C_T/\sigma < 0.12$).

Data Acquisition and Reduction

The imaging system was located in the control room where data was acquired at approximately 5 frames (images) per second and temporarily saved onto two frame grabbers. Shadowgraph images were acquired by synchronizing with the 1P (once per revolution) azimuth pulse from the rotor shaft encoder. Due to the size of each digitized image (369 Kbytes), images were saved onto a microcomputer hard disk on a point by point basis and then backed up post-run onto cartridge disks. During the test, images were examined in real-time and selectively digitized.

Because of restrictions on camera placement, and the resulting limited field of view of the rotor and its wake, the following approach was used to extract the measurement data. Wake geometry was reduced interactively after the completion of the test. The tip vortex coordinates (wake age and radial locations) presented here are based upon measurements scaled and referenced to the blade tip trailing edge. Axial wake geometry is not presented due to the lack of a complete tip path plane reference. The measurement uncertainty of ± 1 pixel corresponds to $\pm 0.30 \text{ cm}$ to 0.45 cm . The range in uncertainty varies depending on the zoom position of the camera.

Results

The feasibility of conducting shadowgraph flow visualization studies on a full-scale rotor was successfully demonstrated. Tip vortex visibility is discussed for the range of operating conditions that were tested. In most cases, the tip vortices were visible for about one complete rotor revolution (four blade passages). Wake geometry results for hover and forward flight and interesting details

of blade/vortex interactions, tip vortices and wake structure are also presented.

Visibility

The visibility of tip vortices was first examined in hover for various M_{tip} conditions ranging from $M_{tip}=0.10$ to 0.605 (50 rpm - 293 design rpm) for 8 deg collective. A previous small-scale shadowgraph rotor test shows that increasing the distance between the shadowgraph screen and camera/strobe location improved the visibility of tip vortices in hover by effectively reducing the camera and strobe offset.³ Shadowgraph results in this full-scale rotor test verified that tip vortices were visible for M_{tip} as low as 0.10 (50 rpm). This is significantly better than that found with small-scale shadowgraph results⁴ which were limited to M_{tip} greater than 0.33 . Also, previous small-scale shadowgraph tests were not very successful in providing top views of the rotor wake. The wake vortex structure was clearly visible during this full-scale test. This greater visibility with full-scale rotors can probably be attributed to the larger vortex core structure. The use of a high power zoom lens during the full-scale test also facilitated visualizing the tip vortices. Improved shadowgraph contrast and visibility were evident as M_{tip} was increased. The capability of visualizing tip vortices at lower than typical M_{tip} conditions can provide greater flexibility in acquiring wake data. In particular, this could be useful for testing low-noise rotor systems with reduced tip speeds.

Hover

Wake geometry data was acquired in hover at $M_{tip}=0.605$ for several thrust conditions. Comparisons between full- and small-scale wake geometry are first presented. Figure 3 shows excellent correlation between the full-scale and 0.16-scale S-76 wake geometry⁴ for the same shaft angle, $\alpha_s=0 \text{ deg}$, and thrust condition, $C_T/\sigma=0.08$. The blades of the 0.16-scale model rotor were dynamically and geometrically similar to the full-scale S-76 main rotor; the model blades, though, had rectangular instead of swept-tapered tips and were tested at a slightly higher $M_{tip}=0.63$. Both rotors show the same rate of radial contraction for their wakes. The full-scale radial wake geometry for four thrust conditions ($C_T/\sigma=0.08, 0.065, 0.05, 0.03$) are presented in Figs. 4-7. Landgrebe's wake model¹⁰, which is empirically derived from small-scale rotor flow visualization data, shows very good agreement with the full-scale rotor wake contraction for each of the thrust conditions.

Forward Flight

A key question prior to the full-scale S-76 rotor test was whether the visibility of the rotor tip vortices would be reduced by the density gradient of the shear flow and turbulent boundary layer on the tunnel walls in forward flight. Results show that acquisition of high quality rotor wake images was possible for a range of rotor operating conditions. A high power zoom lens, however, was required to see the shadowgraphs at the higher advance ratios.

Shadowgraphs were successfully acquired for vertical descent rates and glide slopes as shown in the following figures. Figures 8 and 9 show the radial tip vortex coordinates plotted for the advancing side of the rotor at $\Psi=90$ deg for two flight conditions. These figures also show free-wake geometry predictions derived CAMRAD/JA. The theory correlates well with experimental data for the higher thrust, $C_T/\sigma=0.10$, lower speed condition $\mu=0.10$ (Fig. 8). For the lower thrust, $C_T/\sigma=0.08$, higher speed condition, $\mu=0.15$, however, the free-wake predictions diverge after approximately $\Psi_w=180$ deg (Fig. 9). The CAMRAD/JA free-wake analysis overpredicts the convection of the tip vortex radial trajectory. This is most likely due to the Coanda effect that draws the wake over to the wind tunnel wall. These preliminary results are not conclusive, but are intended to establish the feasibility of the shadowgraph technique for full-scale testing. Further discussion on the effect of ceiling, ground, and wall planes on wake boundaries is referenced.^{6,11}

Blade/Vortex Interactions

Blade/vortex interaction (BVI) noise typically occurs when a helicopter is in a low power descent for landing. In this test entry, all wind tunnel conditions were at low to moderate speeds in which BVI's occurs on both the advancing and retreating sides of the rotor disk. However, shadowgraphs were only taken for the advancing side because the tip vortices on that side of the rotor disk produce greater noise where the relative velocity is higher.

Extremely interesting shadowgraph results on blade/vortex interactions were achieved. Repeatable tip vortex distortions were seen for 11 successive rotor revolutions for the following test condition. Figures 10 and 11 are side view images of the rotor wake for two of these rotor revolutions with the rotor operating at $\alpha_s=10$ deg, $\mu=0.10$, and $C_T/\sigma=0.12$; equivalent to a vertical descent, $V_d=3.7$ m/s (733 ft/min) and glide path angle, $\gamma=10.5$ deg. These figures have been digitally enhanced

for clarity. In both figures, V_∞ is coming from the left with a close-up of the same advancing blade at $\Psi_b=66$ deg. Figures 10 and 11 show the tip vortex trajectories for each of the four blades. These figures show tip vortex "1" trailing from $\Psi_b=66$ deg. Vortex "2", 90 deg wake age later, follows a relatively steady trajectory from $\Psi_b=156$ deg. Vortex "3" shows evidence of a short wave instability in the tip vortex filament from $\Psi_b=246$ deg. This instability lasts for less than 5 deg wake age. Figure 10 shows tip vortex "4" in a spiked trajectory due to a BVI. Figure 11 also shows a severely distorted tip vortex due to a BVI for the same blade. The lack of information on the complete trajectory of tip vortex "4" may be due to a rapid diffusion of the vortex due to the BVI and hence a reduction in visibility using the shadowgraph technique. During this portion of the test, synchronization problems associated with the top camera were being diagnosed, so no top view shadowgraphs for this BVI test condition are available. Nevertheless, it is clear that the shadowgraph technique can, as shown in these figures, provide information on the flow mechanism, location of interactions, and repeatability of the BVI phenomena.

The shadowgraphs in Figs. 10 and 11 were taken at a test condition where there was strong acoustic BVI activity. An independent technique of acoustic signal triangulation indicates possible BVI sources at $\Psi_b=73$ deg near the blade tip, $\Psi_b=76$ deg at 0.86R, and $\Psi_b=77$ deg at 0.82R. An instrumented blade flap gage at 0.70R also revealed a transient down-up pulse at $\Psi_b=72$ deg to 74 deg that is characteristic of a vortex passing beneath the blade. A vortex passing beneath the blade would cause sectional blade lift to decrease and then return to its approximate nominal level prior to the vortex strike. Based on the findings from the acoustic data and dynamic blade response, it is apparent that the shadowgraphs have captured the distorted tip vortex filament caused by a previous blade encounter at approximately $\Psi_b=73$ deg. When the following blade advances, the distorted filament from $\Psi_b=73$ deg has had time (~ 37.5 ms) to convect downstream, and hence be in the vicinity of $\Psi_b=66$ deg.

Figure 12 is an example of predicted azimuthal and radial locations for BVI's on the advancing and retreating side of the rotor for the BVI test condition just noted. The figure shows both a top and side view of predicted BVI strikes with V_∞ coming from the left side of the figure. The largest symbols represent tip vortices closest to the blade. These predictions indicate possible BVI's ranging from $\Psi_b=60$ deg at 0.78R to $\Psi_b=79$ deg at 0.52R. Apparently, these CAMRAD/JA free-wake predictions did a fair job in predicting the general azimuthal locations of BVI's for this test condition.

Detailed Vortex Structure and Tip Vortex Roll-up

Previous shadowgraph results of small-scale rotors have had only sufficient resolution to reveal the tip vortex. In this full-scale rotor test, details of both the primary tip vortex and inboard vorticity sheet were obtained. Such details were visible with the use of a high power zoom lens. Figure 13 is a top view shadowgraph close-up of the advancing side of the rotor blade ($\Psi_b=99$ deg) that was acquired when the rotor was operating at $\alpha_s=10$ deg, $C_T/\sigma=0.12$, $M_{tip}=0.605$, and $V_\infty=6$ knots. The figure shows individual strands of the tip vortex coalescing into one primary tip vortex. The tip vortex roll-up process appears complete within a few degrees of wake age. Excellent details of the inboard vortex sheet are visible as overlapping layers of fluid flow being shed along the trailing edge of the rotor blade. This is evidenced in the right side of the figure as striated lines of vorticity of varying contrast levels. This is apparent when compared to outside of the tip vortex and wake roll-up region. Also, the tip vortex core structure is visible as a dark inner core region surrounded by a brighter periphery. Figure 14 is a side view shadowgraph of the retreating side of the rotor where again the tip vortex core structure and inboard sheet of vorticity are visible. This image was acquired when the rotor was operating at the same shaft angle, thrust coefficient and wind tunnel speed as the previous figure, but at $\Psi_b=259$ deg. In this figure, the blade is moving to the right, with details of the inboard sheet visible below the shed tip vortex. Note the tip vortex appears fully rolled up prior to the trailing edge of the rotor blade. Previous researchers support the observation that the vortex roll-up occurs almost immediately downstream of the wing/blade tip, although the inboard vorticity sheet likely continues to feed into the tip vortex.^{12,13} Figure 15 illustrates a close-up of the tip vortex shed from the blade at $\Psi_b=249$ deg in hover at $C_T/\sigma=0.03$. The blade from which the vortex is shed is just to the right of the tip vortex, but not shown in the figure. Details of the transition from a laminar ($\Psi_w=1.2$ deg) to turbulent tip vortex filament ($\Psi_w=3.4$ deg) are visible in this shadowgraph. The blade root end and its attachment to the pitchcase, shown above the vortex, is actually above and behind the vortex at $\Psi_b=159$ deg.

Many interesting tip vortex features were examined in this test. Figure 16 reveals an apparent double vortex being shed at the tip, a primary tip vortex and a comparatively less visible secondary vortex for an operating condition of $C_T/\sigma=0.09$ and $\mu=0.15$. This was seen in several cases. Previous researchers have observed the existence of a double vortex structure, but that it is unstable which results in the secondary vortex being absorbed by the primary tip vortex.^{14,15} This is what

causes the instability or "kink" in the vortex filament. This characteristic vortex "kink" or instability is shown digitally enhanced in Fig. 17 for $C_T/\sigma=0.11$ in hover. The instability occurs over a range of approximately 40 deg wake age compared to the short wave instability seen in Fig. 10. This "kink" in the tip vortex filament was seen in most close-up shadowgraphs of the rotor in hover and was most likely aggravated by recirculation effects in the wind tunnel. In forward flight, close inspection revealed a very steady tip vortex filament as has been seen in a previous small-scale rotor test.¹

Other vortical behavior was visualized, such as interlocking tip vortices and vortex/vortex interactions as shown in Figs. 18 and 19. Figure 18 shows two vortices intertwined at the rear of the rotor disk ($C_T/\sigma=0.09$ and $\mu=0.20$). This may be due to the initiation of the dual vortex roll-up, downstream of the rotor disk. Figures 19a and 19b are a pair of shadowgraph images that were acquired simultaneously in hover for $C_T/\sigma=0.08$. These figures have been digitally enhanced for clarity. The same vortex is shown in both the side and top views. Three-dimensional coordinates were reduced from the two simultaneously acquired images shown in Fig. 19. The vortex at $\Psi_w=86$ deg (just prior to the leading edge of the following blade), is at a radial and axial location ($r/R, z/R$) of $0.89R$ and $0.03R$, respectively. A vortex/vortex interaction in the first quadrant of the rotor disk is also shown in Fig. 19a. The tightly rolled up vortex trailing from $\Psi_b=80$ deg becomes diffused and remains diffused due to the vortex/vortex interaction.

Summary

The feasibility of conducting full-scale rotorcraft flow visualization research was demonstrated for the first time in the NASA Ames NFAC 80- by 120-Foot Wind Tunnel. The following results are highlighted:

- 1) Full-scale flow visualization, using the wide-field shadowgraph technique, appears relatively straightforward. In this test, the use of a specially developed synchronized imaging system proved very successful in the examination of selected regions of the rotor wake in real-time.
- 2) The wide-field shadowgraph technique is a useful tool in its capability for providing insight into fundamental rotor wake characteristics for a large range of test operating conditions. Overall, tip vortices in this full-scale rotor test were visible for thrust conditions as low as $C_T/\sigma=0.03$ and tip Mach numbers as low as $M_{tip}=0.10$.

- 3) Although, previous small-scale shadowgraph tests have not been very successful in providing top views of the rotor wake, the wake vortex structure was clearly visible during this full-scale test with success in acquiring radial wake geometry for several thrust conditions. This was due to improvements in imaging resolution, zoom lens capability, and improved optics.
- 4) Wake geometry was successfully acquired for selected regions of the rotor wake in hover and forward flight. Empirical wake models correlated well with the hover wake geometry that was acquired. Nonuniform inflow free-wake model predictions were also compared to the forward flight wake geometry.
- 5) Shadowgraphs of blade/vortex interactions were successfully acquired as a preliminary step in supporting rotor aeroacoustics research. Preliminary results indicate good correlation with acoustic noise measurements.
- 6) Indications of tip vortex roll-up, inboard vorticity sheet, tip vortex transition from laminar to turbulent, vortex instabilities, double tip vortices, interlocking vortices, and vortex/vortex interactions were revealed during this test entry.
- 7) Simultaneous acquisition of shadowgraph image pairs was demonstrated as a means for acquiring quantitative three-dimensional wake geometry.
- 8) Finally, further flow visualization studies should be conducted to better assess tip vortex roll-up and wake structure for various scaled rotor systems. Optimizing the camera position in a future test will allow for more accurate determination of the spatial relationship between the tip vortex and blade passage, as well as the spanwise location along the blade where blade/vortex interactions occur.

Acknowledgements

The development and procurement of a special imaging system was made possible by funding through an Ames Center Director's Discretionary Fund for basic research. Special thanks to Joseph Muratore for his invaluable technical assistance and guidance in the development of the synchronized imaging system. The author would also like to recognize the efforts of Patrick Shinoda and David Signor, as Project and Test Directors, for the successful conduct of the S-76 test program. Thanks to Michael Marcoloni for providing the code for extracting BVI predictions and to Johannes van Aken for incorporating his plotting utility in the code. And thanks

to Martin Hagen and Stephen Swanson for assisting the author in the preliminary examination of acoustic results.

References

- ¹Light, J., Swanson, A., and Norman, T., "Application of the Wide-Field Shadowgraph Technique to Helicopters in Forward Flight," *Journal of the American Helicopter Society*, Vol 37, No. 2, April, 1992.
- ²Leishman, J.G. and Bagai, A., "Fundamental Studies of Rotor Wakes in Low Speed Forward Flight using Wide-Field Shadowgraphy," 9th AIAA Applied Aerodynamics Conference, Baltimore, MD, September, 1991.
- ³Swanson, A. and Light, J., "Shadowgraph Flow Visualization of Isolated Tiltrotor and Rotor/Wing Wakes," 48th Annual Forum of the American Helicopter Society, Washington, D.C., June, 1992.
- ⁴Norman, T. and Light, J., "Rotor Tip Vortex Geometry Measurements Using the Wide-Field Shadowgraph Technique," 4th AIAA Applied Aerodynamics Conference, San Diego, CA, June, 1989.
- ⁵Norman, T. and Light, J., "Application of the Wide-Field Shadowgraph Technique to Rotor Wake Visualization," 15th European Rotorcraft Forum, Amsterdam, September, 1989.
- ⁶Light, J., "Tip Vortex Geometry of a Hovering Helicopter Rotor in Ground Effect," *45th Annual Forum of the American Helicopter Society*, Boston, MA, May, 1989.
- ⁷Shinoda, P.M., "Modern Four-Bladed Rotor Research in the NASA Ames 80- by 120-Foot Wind Tunnel," 11th AIAA Applied Aerodynamics Conference, Monterey, CA, August, 1993.
- ⁸Johnson, W., *A Comprehensive Analytical Model of Rotorcraft Aerodynamics and Dynamics*, Johnson Aeronautics Version, Palo Alto, CA, 1988.
- ⁹Martin, R.M., Marcoloni, M.A., Splettsstoesser, W.R., and Schultz, K.J., "Wake Geometry Effects on Rotor Blade-Vortex Interaction Noise Directivity," NASA TP 3015, November, 1990.
- ¹⁰Landgrebe, A., "The Wake Geometry of a Hovering Rotor and its Influence on Rotor Performance,"

Journal of the American Helicopter Society, Vol. 17, No. 4, October, 1972.

¹¹Rossow, V.J., "Effect of Ground and Ceiling Planes on Shape of Energized Wakes", 11th AIAA Applied Aerodynamics Conference, Monterey, CA, August, 1993.

¹²Chow, J.S., Zilliac, G.G., and Bradshaw, P., "Measurements in the Near-Field of a Turbulent Wingtip Vortex," 31st Aerospace Sciences Meeting & Exhibit, January, 1993.

¹³Chigier, N.A. and Corsiglia, V.R., "Tip Vortices - Velocity Distributions," NASA TM X-62,087, September, 1971.

¹⁴Green, S.I. and Acosta, A.J., "Unsteady Flow in Trailing Vortices," *Journal of Fluid Mechanics*, Vol. 227, 1991, pp. 107-134.

¹⁵Thompson, D.H., "A Flow Visualization Study of Tip Vortex Formation," ARL-Aero-Note-421, 1983.

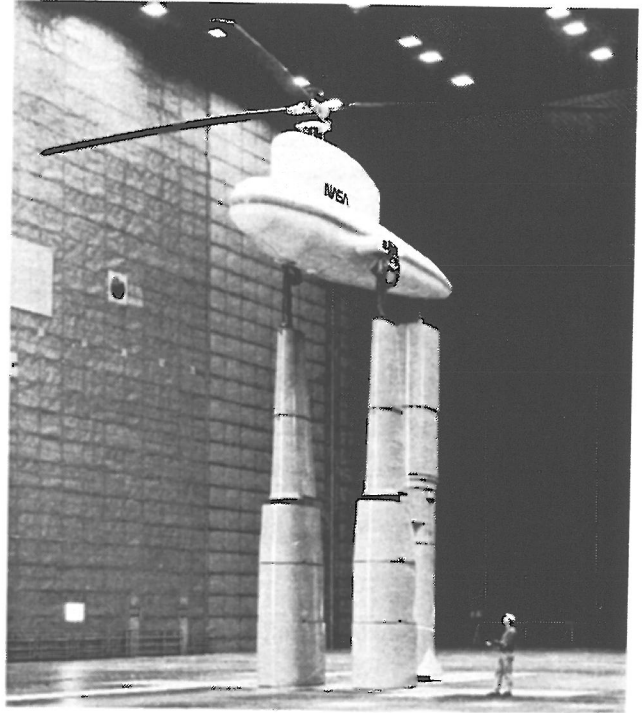


Fig. 1 S-76 rotor in the 80- by 120-Foot Wind Tunnel.

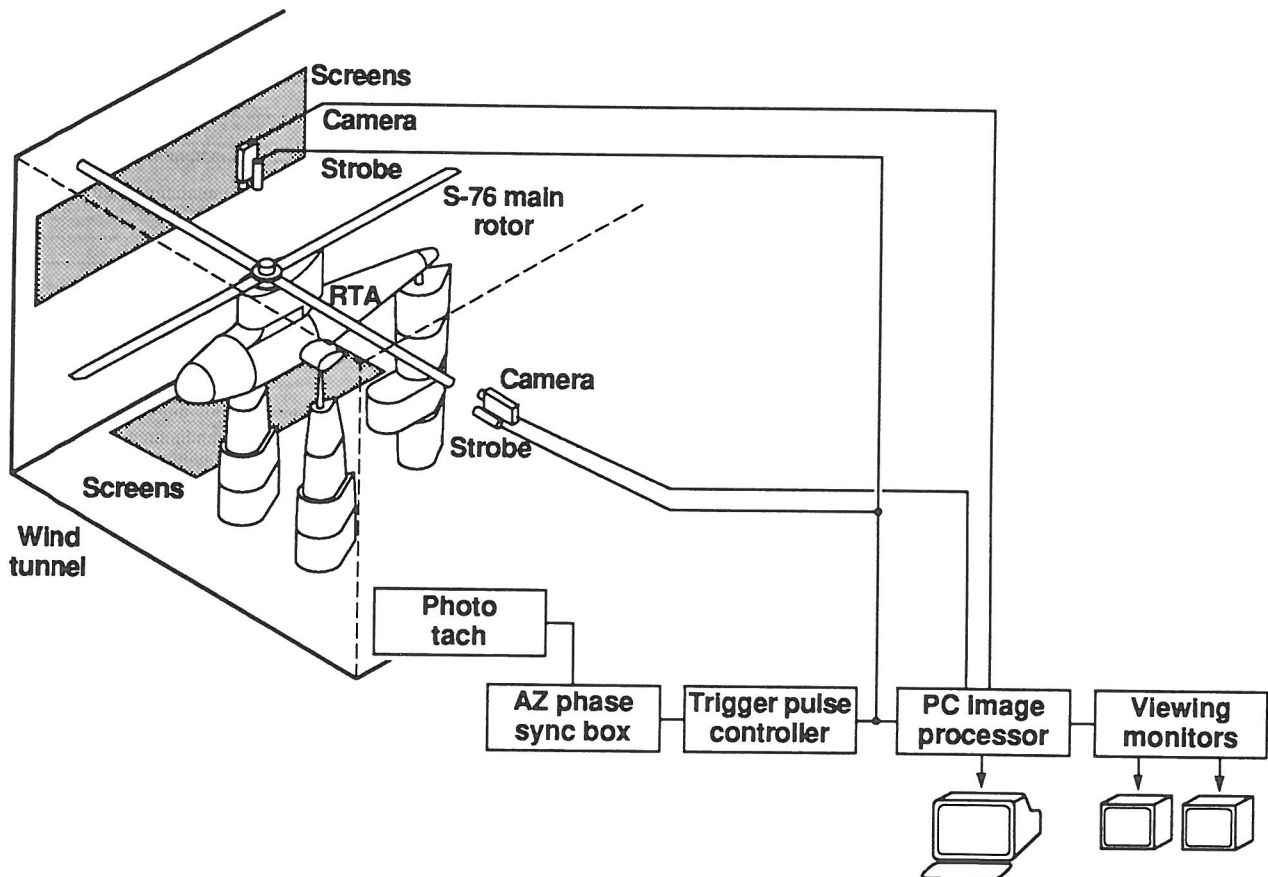


Fig. 2 Experimental set-up for flow visualization and data acquisition.

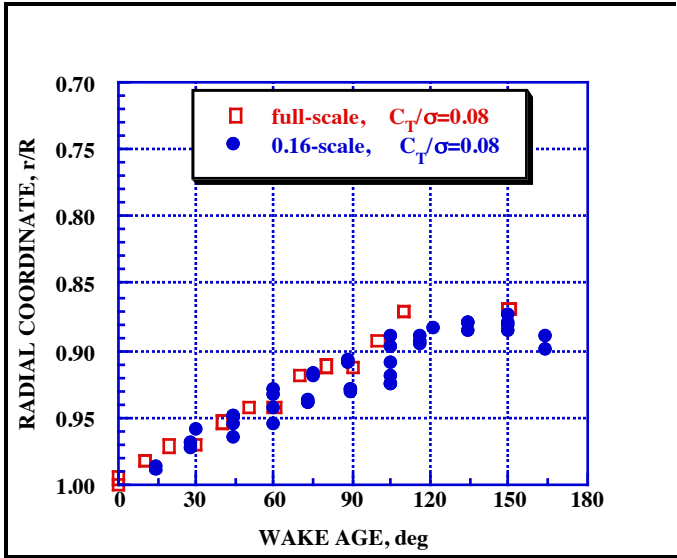


Fig. 3 Full-scale and 0.16-scale S-76 wake geometry in hover; $C_T/\sigma=0.08$.

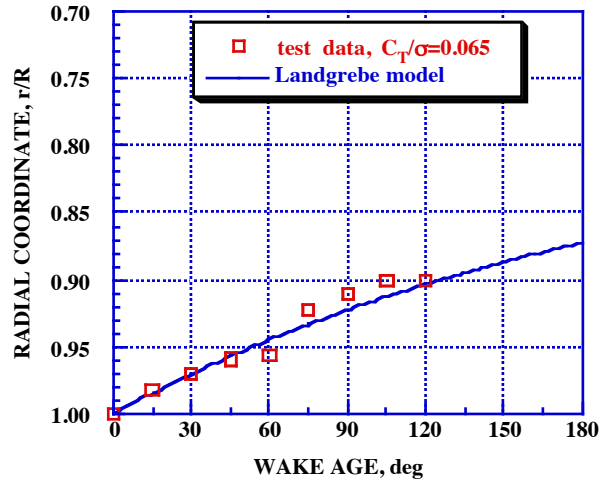


Fig. 5 Landgrebe's empirical wake model with radial wake geometry in hover; $C_T/\sigma=0.065$, $M_{tip}=0.605$.

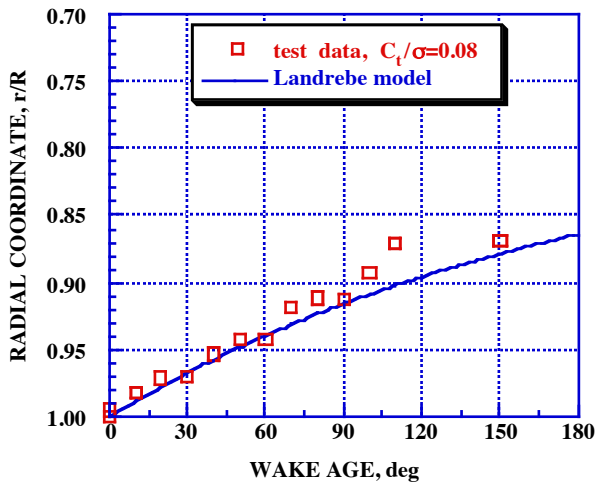


Fig. 4 Landgrebe's empirical wake model with radial wake geometry in hover; $C_T/\sigma=0.08$, $M_{tip}=0.605$.

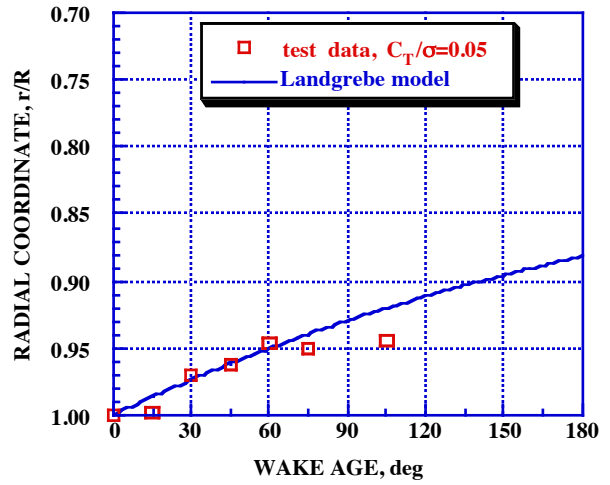


Fig. 6 Landgrebe's empirical wake model with radial wake geometry in hover; $C_T/\sigma=0.05$, $M_{tip}=0.605$.

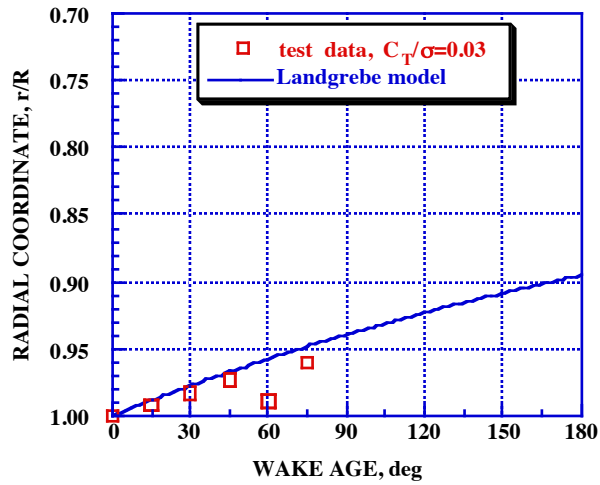


Fig. 7 Landgrebe's empirical wake model with radial wake geometry in hover; $C_T/\sigma=0.03$, $M_{tip}=0.605$.

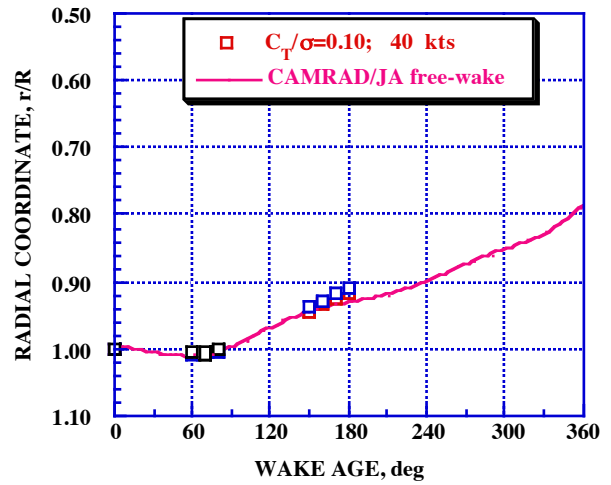


Fig. 8 CAMRAD/JA free-wake calculations with radial wake geometry in forward flight; $C_T/\sigma=0.10$, $\mu=0.10$ (40 kts), $\alpha_s=5$ deg, $M_{tip}=0.605$, $V_d=1.8$ m/s (351 ft/min), $\gamma=5.0$ deg.

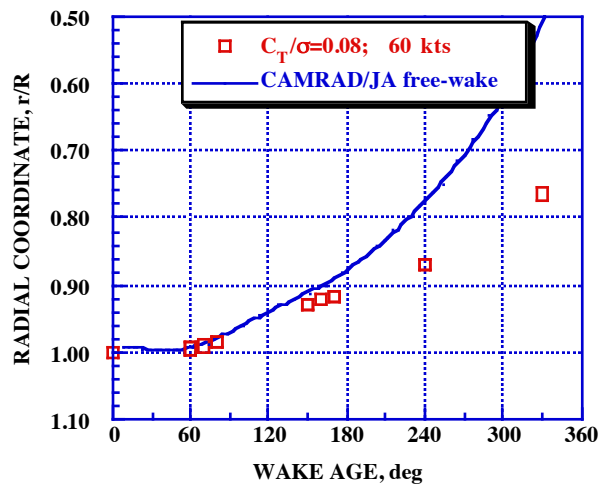


Fig. 9 CAMRAD/JA free-wake calculations with tip vortex radial trajectory in forward flight; $C_T/\sigma=0.08$, $\mu=0.15$ (60 kts), $\alpha_s=5$ deg, $M_{tip}=0.605$, $V_d=1.3$ m/s (257 ft/min), $\gamma=2.4$ deg.

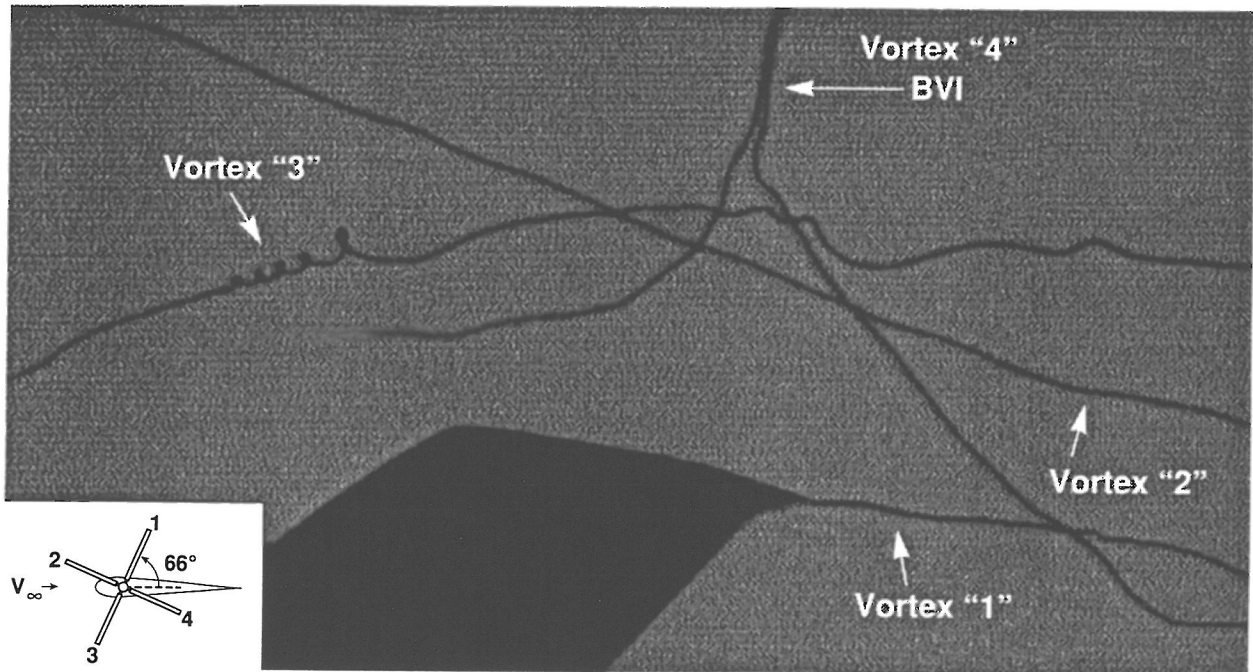


Fig. 10 BVI; $C_T/\sigma=0.12$, $\mu=0.10$, $\alpha_s=10$ deg, $M_{tip}=0.605$, $\Psi_b=66$ deg, $V_d=3.7$ m/s (733 ft/min), $\gamma=10.5$ deg.

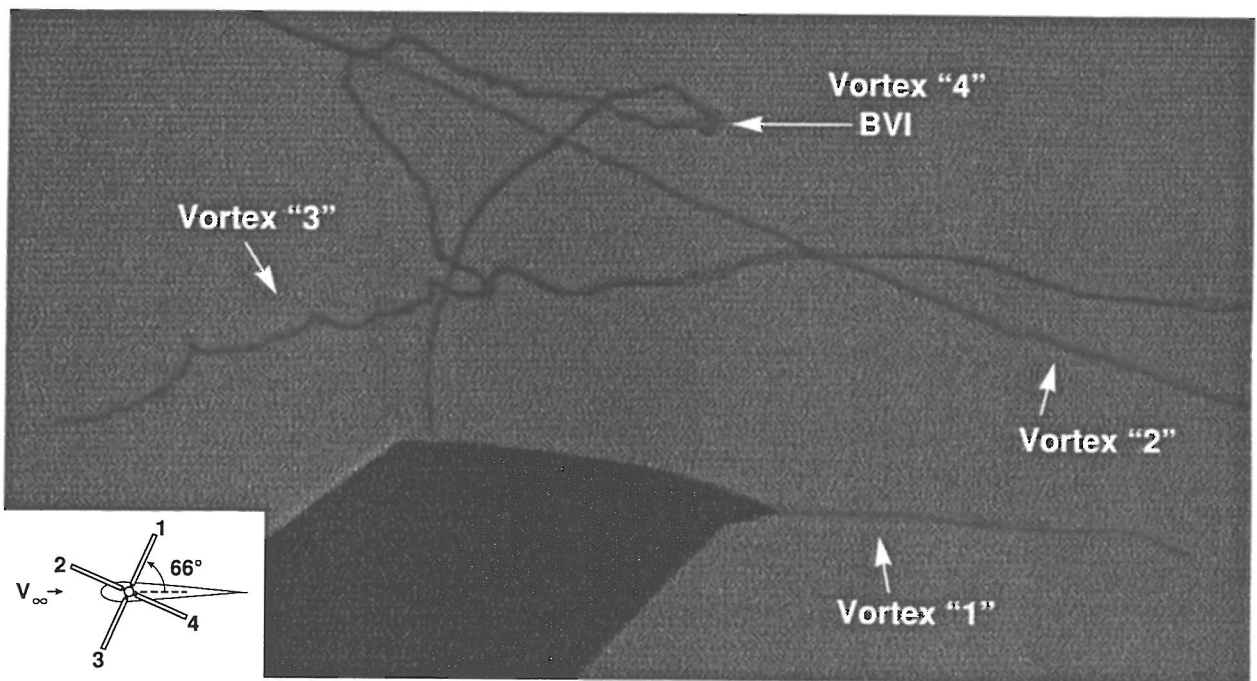


Fig. 11 BVI; $C_T/\sigma=0.12$, $\mu=0.10$, $\alpha_s=10$ deg, $M_{tip}=0.605$, $\Psi_b=66$ deg, $V_d=3.7$ m/s (733 ft/min), $\gamma=10.5$ deg.

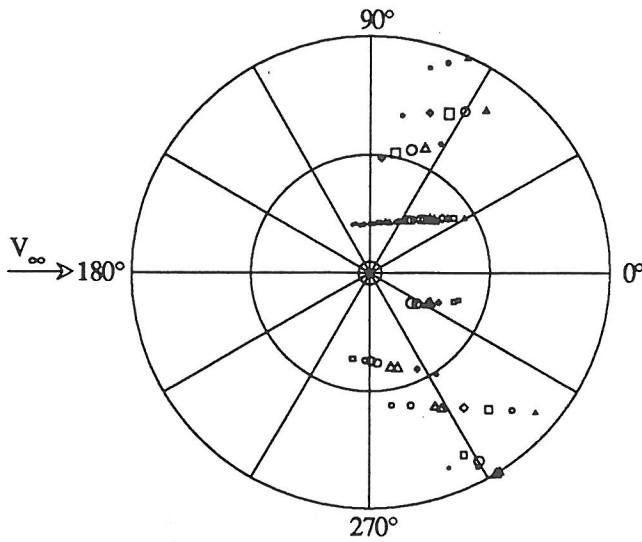


Fig. 12a Top view CAMRAD/JA predictions of potential BVI locations on the advancing and retreating side of the rotor disk; $C_T/\sigma=0.125$, $\mu=0.10$, $\alpha_s=10$ deg, $M_{tip}=0.605$.

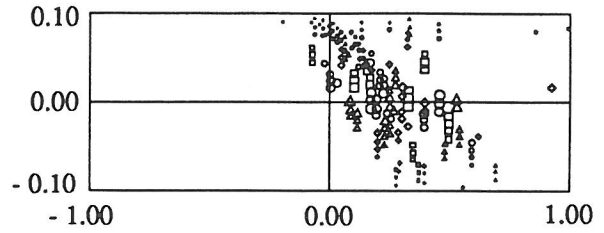


Fig. 12b Side view CAMRAD/JA predictions of potential BVI locations; $C_T/\sigma=0.125$, $\mu=0.10$, $\alpha_s=10$ deg, $M_{tip}=0.605$.

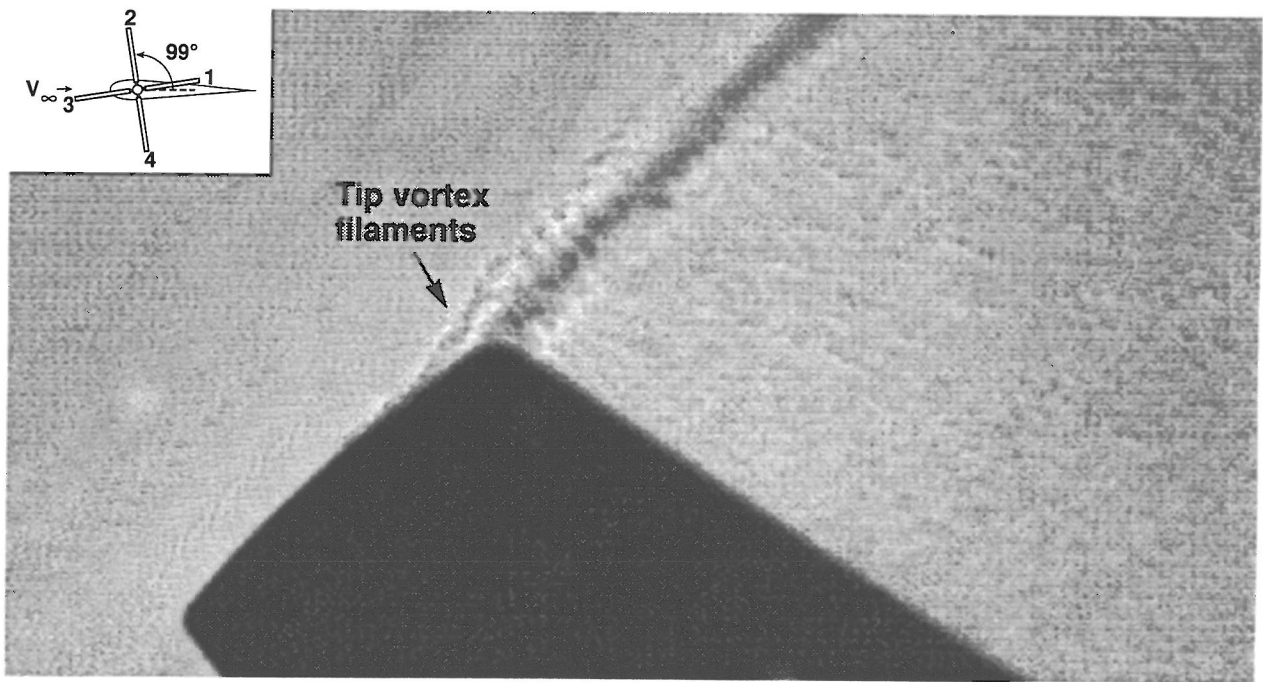


Fig. 13 Top view shadowgraph, $C_T/\sigma=0.12$, $\mu=0.015$, $\alpha_s=10$ deg, $M_{tip}=0.605$, $\Psi_b=99$ deg.

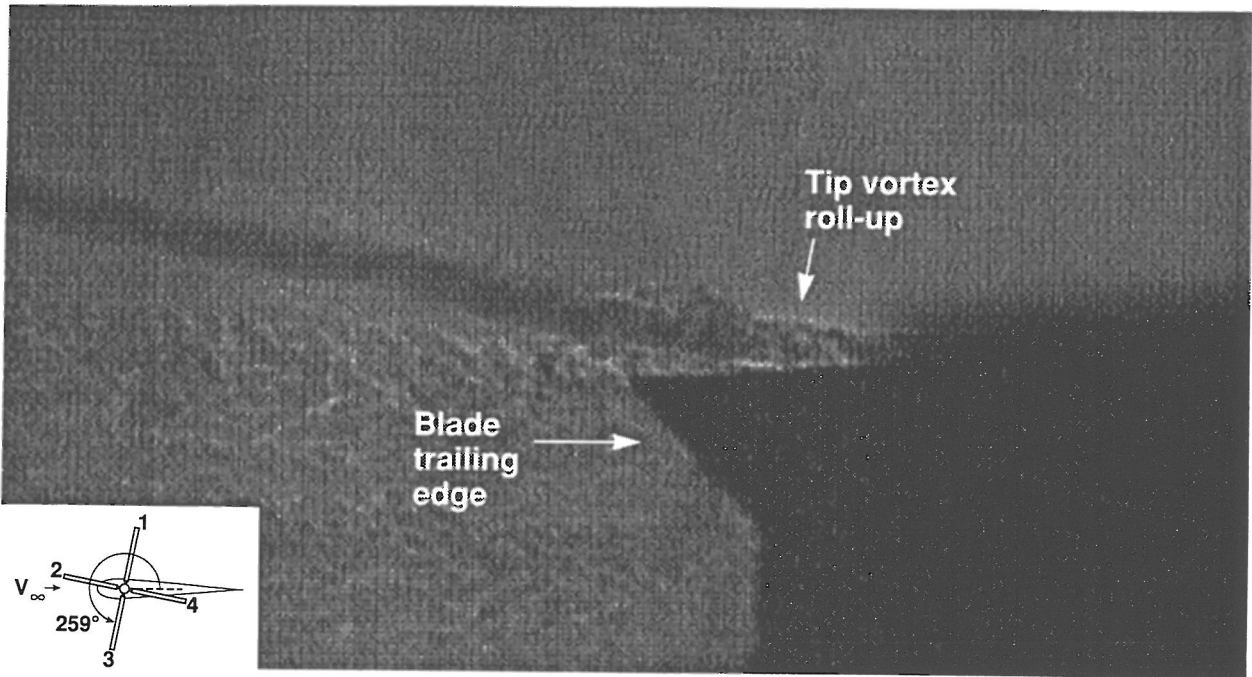


Fig. 14 Side view shadowgraph, $C_T/\sigma=0.12$, $\mu=0.015$, $\alpha_s=10$ deg, $M_{tip}=0.605$, $\Psi_b=259$ deg.

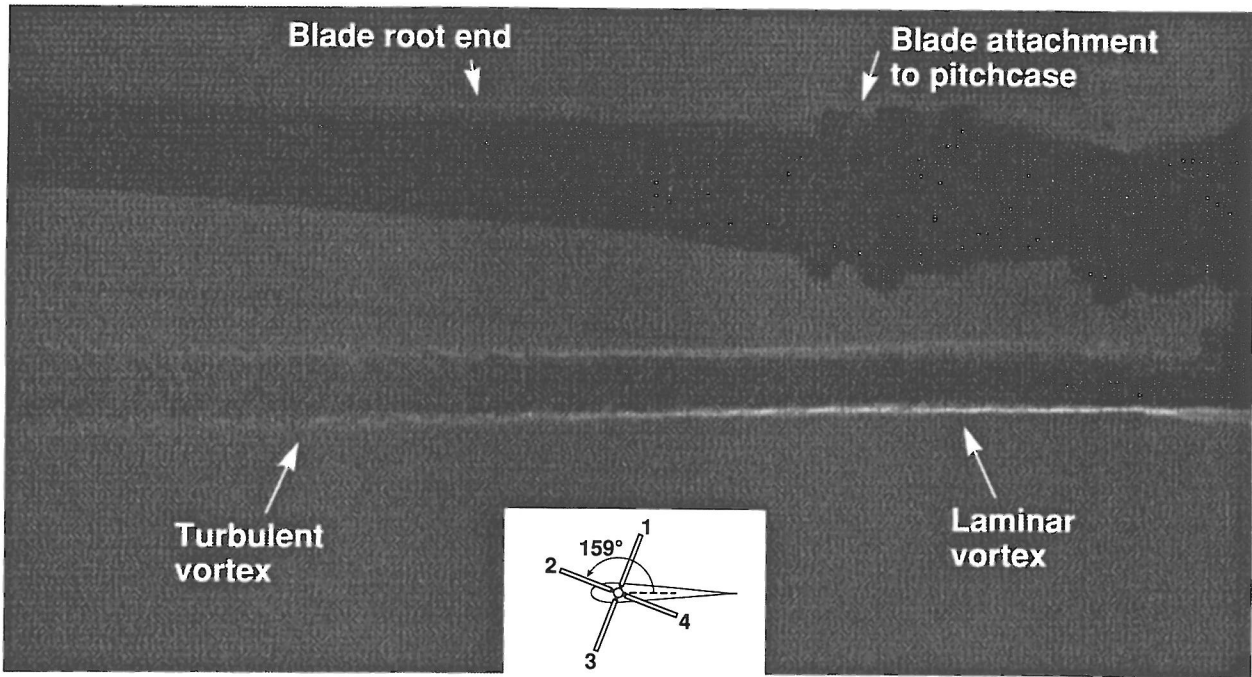


Fig. 15 Tip vortex transition from laminar to turbulent, $\Psi_w=1.2$ deg to 3.4 deg, $C_T/\sigma=0.03$, $\mu=0.0$, $\alpha_s=5$ deg, $M_{tip}=0.605$.

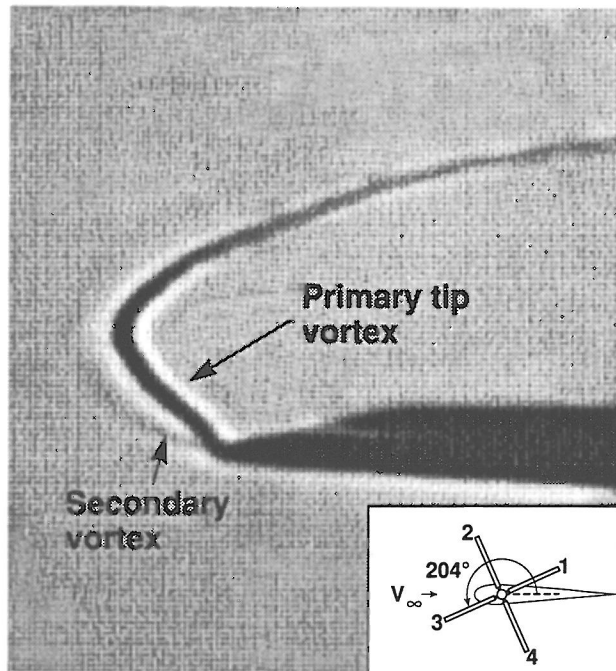


Fig. 16 Double tip-vortex rollup, $C_T/\sigma=0.09$, $\mu=0.15$, $\alpha_s=-2$ deg, $M_{tip}=0.605$, $\Psi_b=204$ deg.

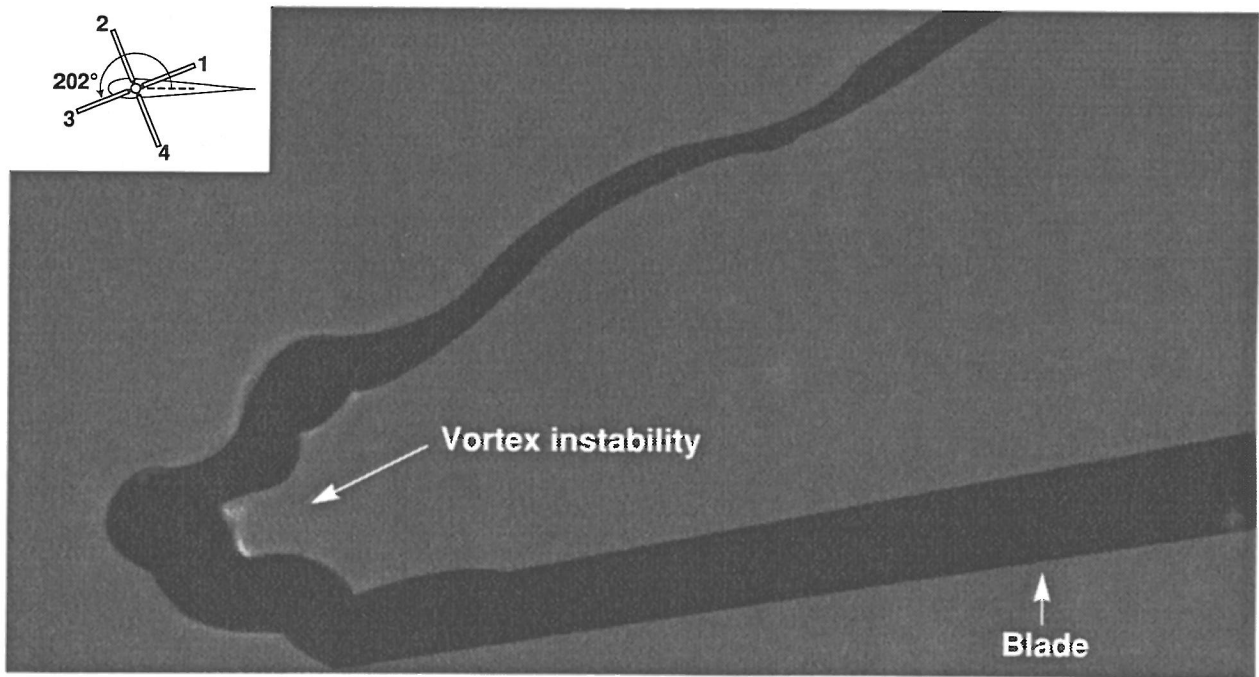


Fig. 17 Close-up shadowgraph of vortex instability, $C_T/\sigma=0.11$, $\mu=0.0$, $\alpha_s=-15$ deg, $M_{tip}=0.605$, $\Psi_b=202$ deg.

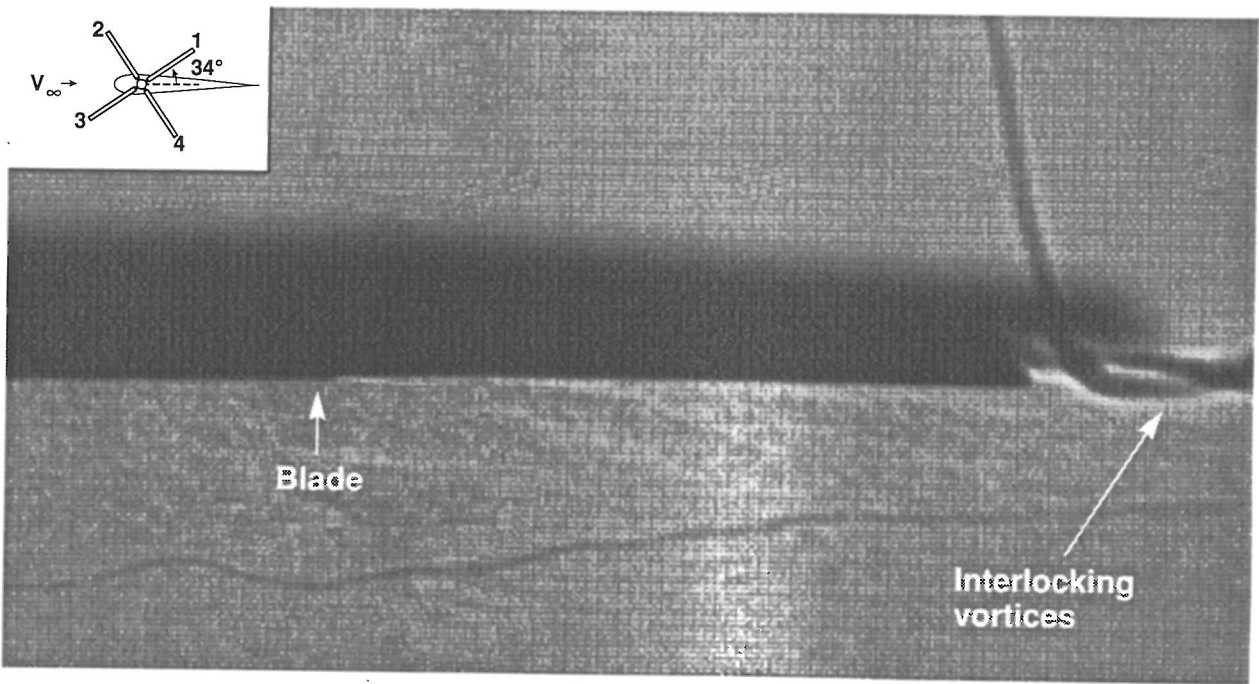


Fig. 18 Interlocking tip vortices, $C_T/\sigma=0.09$, $\mu=0.20$, $\alpha_s=5$ deg, $M_{tip}=0.605$, $\Psi_b=34$ deg.

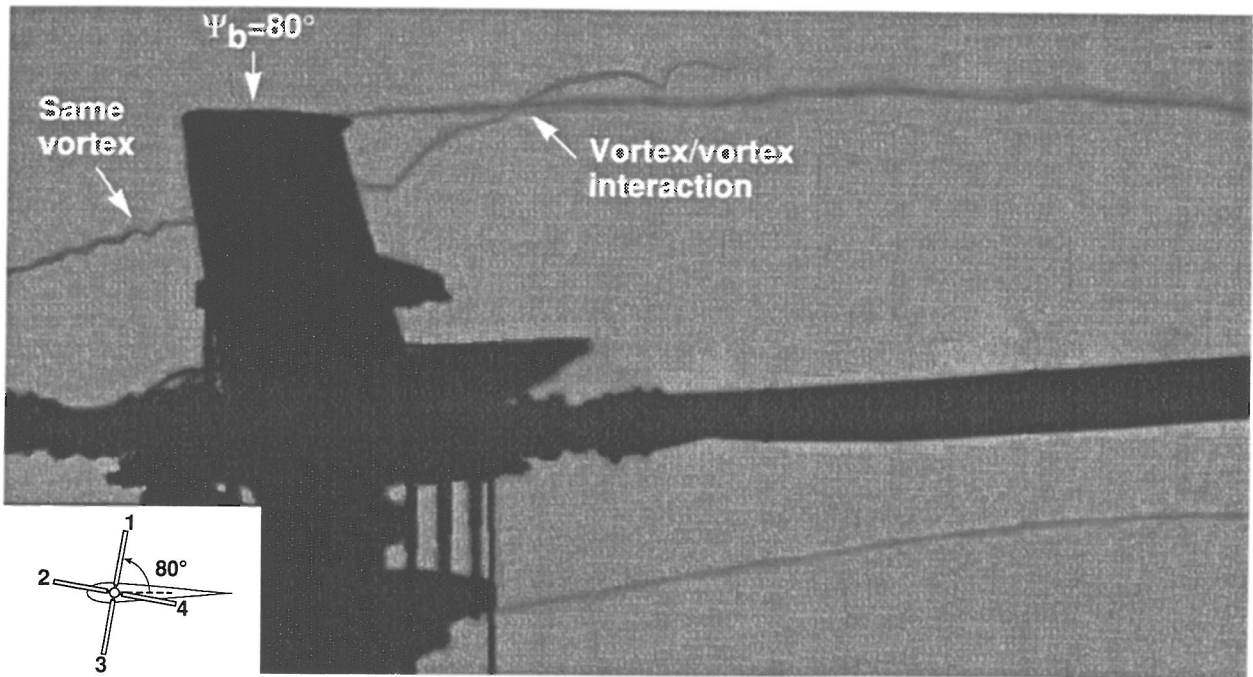


Fig. 19a Side view shadowgraph of same vortex in Fig. 19b at $\Psi_w=86$ deg; also vortex/vortex interactions in first quadrant of rotor disk, $C_T/\sigma=0.08$, $\mu=0.0$, $\alpha_s=0$ deg, $M_{tip}=0.605$; top blade is positioned at $\Psi_b=80$ deg.

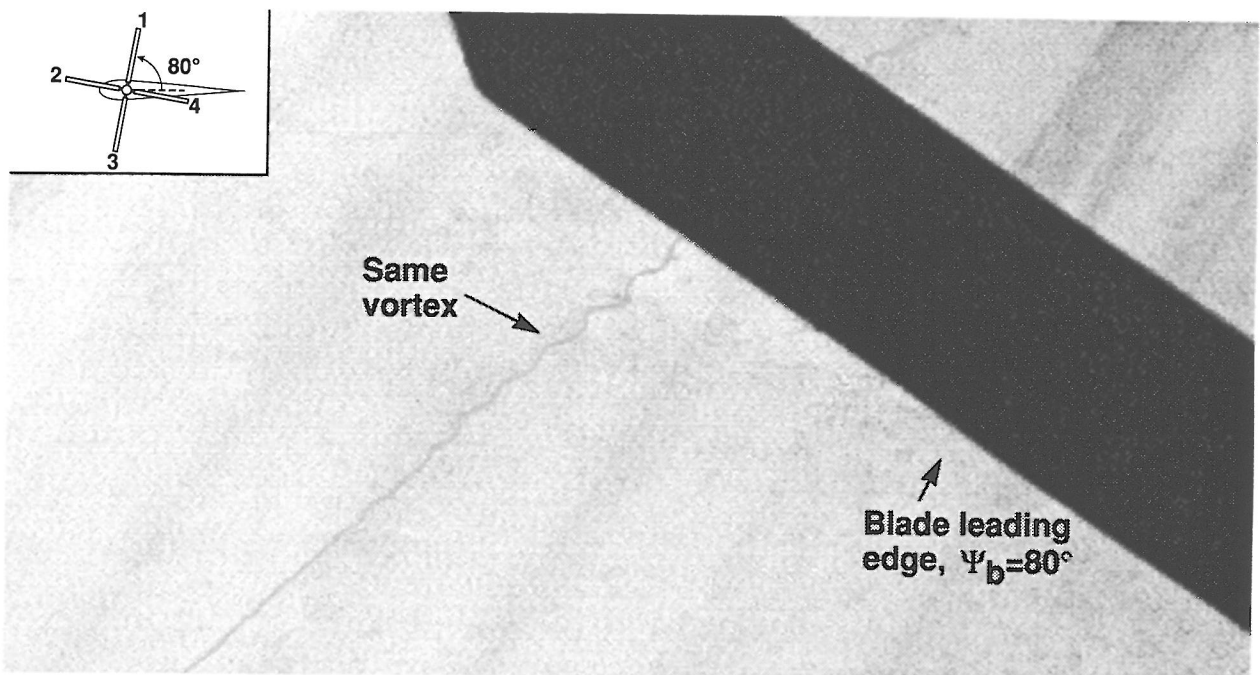


Fig. 19b Top view shadowgraph of same vortex as Fig. 19a at $\Psi_w=86$ deg, $C_T/\sigma=0.08$, $\mu=0.0$, $\alpha_s=0$ deg, $M_{tip}=0.605$; blade is positioned at $\Psi_b=80$ deg.